Effect of heat treatments on fabricated Wire and arc additive manufacturing parts of Stainless steel 316: Microstructure and synchrotron X-ray Diffraction analysis

Authors: Tiago A.Rodrigues [a*] , J. D. Escobar [d], Jiajia Shen [a], Valdemar R. Duarte [a], G. G. Ribamar [b], Julian A. Avila [b], Emad Maawad [c], Norbert Schell [c], , Telmo G. Santos [a], J. P. Oliveira [a ,1, #]

[a] *UNIDEMI, Department of Mechanical and Industrial Engineering, NOVA School of Science and Technology, Universidade NOVA de Lisboa, 2829-516 Caparica, Portugal*

[b] *São Paulo State University (UNESP), Campus of São João da Boa Vista, Av. Profª Isette Corrêa Fontão, 505, Jardim das Flores, 13876-750, São João da Boa Vista, SP, Brazil*

[c] *Helmholtz-Zentrum Geesthacht, Institute of Materials Research, Max-Planck-Str. 1, Geesthacht, 21502, Germany*

[d] *Metallurgical and Materials Engineering Department, University of São Paulo, Av.Prof. Mello Moraes 2463, 05508-030, São Paulo, SP, Brazil*

*Corresponding author at tma.rodrigues@campus.fct.unl.pt

Corresponding author at jp.oliveira@fct.unl.pt

Abstract

Different geometrical features and intricate parts can now be fabricated by wire and arc additive manufacturing (WAAM). Even though a broad range of applications rises with this technology, the processed metallic materials still follow metallurgy rules. Therefore, undesired phases may appear during the multiple thermal cycles affecting the fabricated part. One of the most used stainless steel in the industry is the 316L, which provides a combination of high corrosion resistance and mechanical properties. In this study, 316L stainless steel walls were fabricated by WAAM and submitted to several heat treatments to understand the precipitation kinetics of secondary phases and observe the δ-ferrite dissolution with synchrotron X-ray diffraction measurements. The as-built samples presented δ-ferrite dendrites in an austenite

---

[1] **Statement on Conflicts of Interest**: One of the authors of this article is part of the Editorial Board of the journal. To avoid potential conflicts of interest, the responsibility for the editorial and peer-review process of this article lies with the journal's other editors. Furthermore, the authors of this article were removed from the peer review process and had no, and will not have any access to confidential information related to the editorial process of this article.

(γ) matrix. In-situ observations showed σ precipitation during the first minutes of isothermal holding at 950 °C, from direct precipitation on the δ-ferrite islands. Solubilization heat treatments at 1050 and 1200 °C resulted in an undissolved amount of ferrite of approximately 6.5 % and 0.4 %, respectively. The amount of δ-ferrite showed a direct relationship with the hardness values. This work combined advanced materials characterization and thermodynamic calculations to rationalize the microstructure evolution upon the use of heat treatments in WAAM-fabricated 316L stainless steel parts.

Keywords: wire and arc additive manufacturing; stainless steel; sigma phase; in-situ phase transformation, high energy synchrotron x-ray diffraction

Graphical Abstract

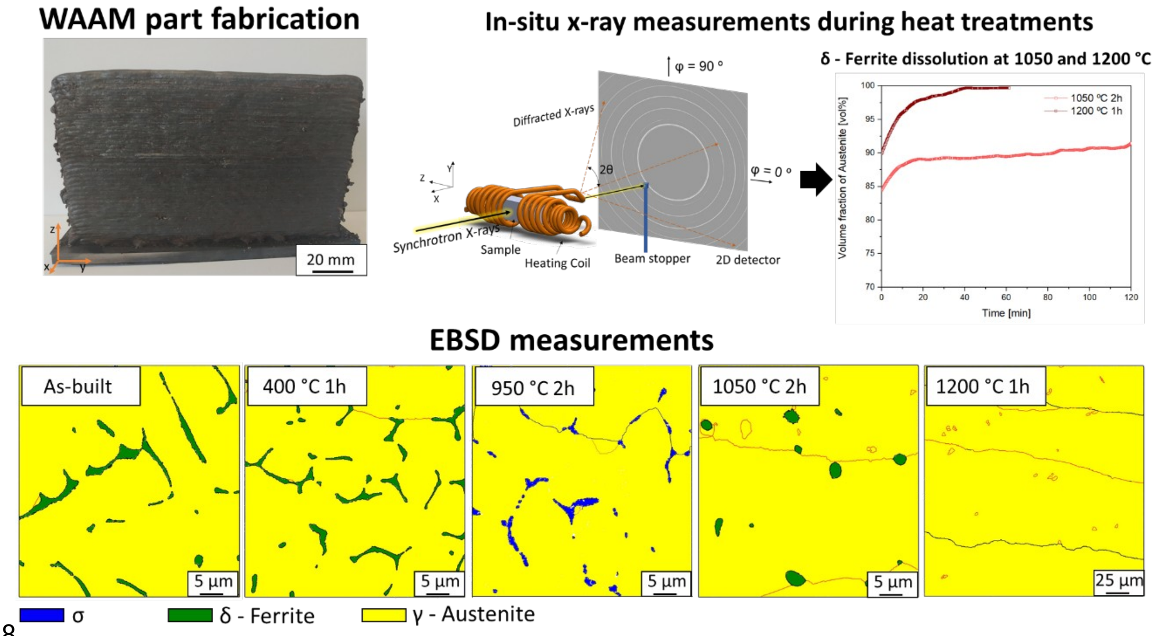

Highlights

- Different heat treatments were performed on stainless steel 316L WAAMed parts
- σ precipitation is observed in-situ via high energy synchrotron X-ray diffraction
- σ starts to precipitate during the first minutes of isothermal holding at 950 °C in the δ-ferrite grains
- The amount of δ-ferrite decreased with an increase in the solubilization temperature.
- Eddy current testing is capable to differentiate δ-ferrite and σ.

1. Introduction

Austenitic stainless steels are widely used in several industrial applications where exceptional corrosion resistance and excellent mechanical properties at elevated temperatures is a requirement, including nuclear energy [1,2] petrochemical, and chemical industries [3]. For example, parts from a reactor core in nuclear applications are exposed to high strength and corrosion environments at operating temperatures between 280-550°C [4,5]. The mechanical strength of austenitic stainless steels is reduced considerably above 500°C [6], and the fatigue crack propagation accelerates under operational temperatures above 150°C [7]. Austenitic stainless steels are also an economical structural material used for marine and biomedical applications [8,9].

Stainless steels are relatively expensive to machine from a billet, therefore complex parts are more feasible and cheaper to fabricated with additive manufacturing technologies. Regarding additively manufactured samples of austenitic stainless steels, Lou et al. [10] highlight the necessity of producing an equiaxed microstructure through high-temperature recrystallization annealing, which increases the corrosion fatigue resistance.

Wire and arc additive manufacturing (WAAM) is a variant within the metal additive manufacturing group, based on the fundamentals of arc welding [11], where a wire feedstock material is melted by an electric arc and deposited in a layer-by-layer fashion. WAAM features high deposition rates and high material efficiency (less material waste), which is interesting for building large components for industrial applications, such as for the oil and gas, and nuclear sectors.

Austenitic stainless steels manufactured by WAAM typically exhibit δ-ferrite dendrites within an austenitic (γ) matrix [12]. Some authors found that δ-ferrite can prevent hot cracking by accommodating large amounts of pure S and P in the interdendritic areas [13–16] while also acting as a strengthener. The multiple heating/cooling cycles experienced during WAAM of austenitic stainless steel, combined with the long soaking times at high temperatures, affect the microstructure evolution in WAAM fabricated parts, and can result in the formation of undesired secondary phases [17]. When austenitic stainless steels experiences low cooling rates and long times between 550-900 °C, Cr-rich carbides ($M_{23}C_6$ and M_7C_3) [18] will form, as well as the potential for precipitating intermetallic deleterious phases increases, such as sigma (σ) [19], chi (χ) [20–22], and Laves [18]. Especially regarding WAAM, it has been largely reported that the as-fabricated microstructures in austenitic stainless steels, as a result of microsegregation of Cr during solidification can contain σ [23,24]. depending on the process parameters and location within the sample. The σ phase leads to hardening and embrittlement in stainless steel and therefore has received particular attention [25,26]. In addition, σ consumes chromium and molybdenum from the austenite matrix, deteriorating its corrosion resistance [27].

The solidification conditions and multiple heating/cooling cycles during fusion based additive manufacturing can render different microstructure features when compared to conventionally used processes such as casting. The commonly used heat-treatments for welding and wrought material may also need to be adapted when producing WAAM parts. Some authors [28] have suggested that at 950 °C δ-ferrite could dissolve without the precipitation of secondary phases after post-weld heat treatment. As it will be shown in this work, the same heat treatment condition when applied to the WAAM 316L stainless steel parts will render different microstructure features.

It has been also discussed that δ-ferrite can serve as nucleation sites for the precipitation of $M_{23}C_6$ and σ upon annealing cycles around 720 °C. However, proper annealing cycles around 1050 °C can provide complete dissolution of δ-ferrite, avoiding the formation of secondary precipitates [29]. The presence of compositional segregations and δ-ferrite are mostly unavoidable and therefore understanding the microstructural evolution of as-built austenitic stainless steels after WAAM heat treatment is currently a topic of great interest for the additive manufacturing community. In-situ synchrotron X-ray diffraction measurements are especially useful in this case to understand the kinetics of phase transformations during heat treatments.

This study investigates the phase transformations in a 316L austenitic stainless steel after WAAM using synchrotron X-ray diffraction. The kinetics of δ-ferrite dissolution was studied during post-WAAM heat treatment at 400, 950, 1050, and 1200 °C. The selection of these heat treatments was made base on the literature [23,30–32]. Complementary EBSD analysis was performed to confirm the morphology, size, and distribution of δ-ferrite and σ before and after heat treatment. Eddy's current testing was used to highlight that δ-ferrite can be distinguished from σ with this technique. While hardness and electrical conductivity measurements were used to demonstrate the differences that each phase can have on the final properties of the processed materials. Our observations provide a new understanding of the effects of time and temperature on the microstructural evolution of as-built austenitic stainless steels after WAAM and provide auseful guide to design or optimize heat treatment routes relevant to additively manufactured parts.

2. Materials and methods

2.1 Experimental setup

In this study, WAAM single-walls were fabricated using an in-house custom-made WAAM apparatus, which included a customized gas metal arc welding (GMAW) torch. The wire feedstock used in this work was a commercial 316L stainless steel wire (ER 316LSi) with a diameter of 1 mm. The chemical composition of the feedstock wire is detailed in Table 1. A WAAM wall with 180 x 110 x 8 mm was built with a wire feed speed of 4 m/min and a travel speed of 300 mm/min. A voltage of 19.5 V was used, and the molten pool was protected with 99.99 % Argon. A zig-zag deposition strategy with 90 seconds of idle time between each torch stop/start was selected to build the 75-layer WAAM part.

Table 1 - Chemical composition of the ER 316LSi wire electrode (wt.%).

C	Mn	Si	Ni	Cr	Mo	Cu	Fe
0.03	1.60	0.65	11	18.5	2.50	0.75	Bal.

2.2 In-situ synchrotron x-ray diffraction during heat treatments

Four post-WAAM heat treatments (PWHT) were performed in-situ at the High Energy Materials Science beamline at PETRA III, DESY (Hamburg, Germany) with a beam energy of 100 keV (0.1234 Å). Material expansion/shrinkage during heating and cooling was measured using a modified Bähr DIL-805 dilatometer filled with Argon to avoid oxidation during the heat treatments.

The four different heat treatments were performed as follows: HTT#1 consisted of a stress relief heat treatment at 400 °C for 1 hour, followed by air cooling; HTT#2 aimed at promoting σ precipitation and was performed at 950 °C for 2 hours, followed by forced gas (Ar) cooling; HTT#3 was performed at 1050 °C for 2 hours, followed by forced gas (Ar) cooling; while HTT#4 was performed at 1200 °C for 1 hour, also followed by forced gas (Ar) cooling. It should be noticed that the selection of imposing forced gas cooling aimed at avoiding the precipitation of intermetallics after the termination of the high-temperature plateau. All conditions were heated up to the target treatment temperature at a rate of 20 °C/s. As for the cooling conditions, HTT#1 had a cooling rate of 5 °C/s, while for the remaining heat treatments, a cooling rate of 20 °C/s was imposed.

A schematic representation of the heat treatments performed and the in-situ setup used are depicted in Figure 1 and Figure 2. The primary purpose of the synchrotron experiments was to determine the δ-ferrite dissolution and the kinetics of secondary phase formation/dissolution during the selected heat treatments.

A 2D Perkin Elmer detector with a pixel size of 200 µm was used to capture the Debye-Scherrer diffraction rings. These were then integrated along the full azimuthal angle (ϕ) using freely available Fit2D software [33] to obtain conventional (Intensity vs. d-spacing) diffraction patterns. The beam size was 1 x 1 mm, and the sample-to-detector distance was set to 1517 mm. LaB_6 calibrant powder was used to estimate the instrumental peak broadening associated with the beamline, and the exposure time was set to 5 seconds. During the in-situ measurements, dark images were also acquired and subtracted to reduce the noise of the detector images.

An in-house python-based routine was used to fit the diffraction peaks. The python routine used a Python package named *xrdfit [34]*, which implemented a *Pseudo-Voigt* profile function to fit peaks and extract the analyzed data in this study, i.e., the peak position, full width half maximum, and area under the fitted peaks. This information was then used to quantify the current phases at any given point during the heat treatments, following Escobar et al.[35] methodology. The austenite and ferrite volume fractions were measured using equations (1) and (2). F_p is the fraction of austenite/ferrite, n_p is the number of peaks of austenite/ferrite considered, k represents each {hkl} family/peak, I_{pK} the intensity of each peak, and R_{pK} is a scalar containing the effect of the remaining parameters: theoretical cell volume (V_p), the multiplicity of the peak (M), and the structure factor (Fk) of the {hkl} plane family. The R_{pK} was calculated for all presented phases of austenite and ferrite. The peaks tracked were: δ {220}, γ {222}, γ {311},δ {211},γ {220},δ {200},γ {200},δ {110},γ {111}. The final volume fraction of austenite was calculated following equation (3). This method to quantify the volume fraction of each phase was compared with actual Rietveld refinements measurements, using MAUD software [36]. The lattice strain for certain (h k l) peaks was calculated accordingly equation (4). The d-spacing of the as-built sample was considered as d_0.

$$F_p = \frac{\frac{1}{n_p}\sum_{K}^{n_{pk}} \frac{I_{pk}}{R_{pk}}}{\sum_p \frac{1}{n_p}\sum_{K}^{n_{pk}} \frac{I_{pk}}{R_{pk}}} \tag{1}$$

$$R_{pK} = \frac{{F_k}^2 \times M}{{V_p}^2} \tag{2}$$

$$F_{p_{austenite}} = \frac{F_{p_{austenite}}}{F_{p_{austenite}} + F_{p_{ferrite}}} \tag{3}$$

$$Lattice\ strain_{hkl} = \left(\frac{d - d_0}{d_0} \times 10^6 \right)_{hkl} \tag{4}$$

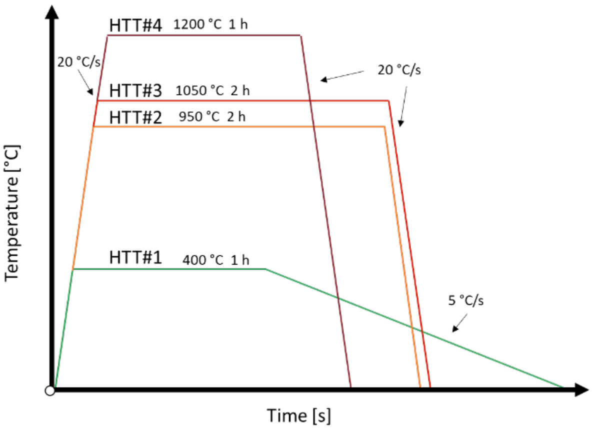

Figure 1 - Schematic representation of the heat treatments applied during In-situ Synchrotron X-ray diffraction measurements. The time-temperature plot also resumes the heating and cooling ramps used.

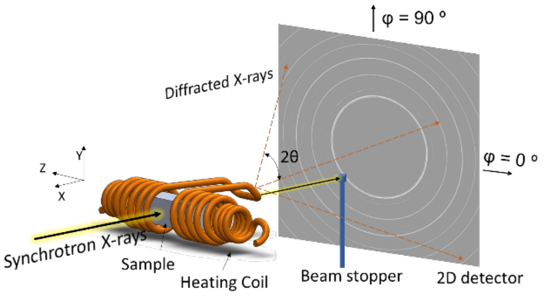

Figure 2 - Schematic representation of the experimental setup applied to perform the in-situ heat treatments.

2.3 Microstructural characterization

All conditions, including the as-built WAAM walls, were analyzed via optical and scanning electron microscopy, hardness testing, and electrical conductivity measurements. For the microscopy observations, samples were polished using abrasive papers with grit from 80 to 2000 and polished using a 3 µm diamond suspension. Vilella's reagent was used to reveal the microstructure. A Leica DMI 5000 M optical microscope and an FEI Quanta FEG – Inspect-F50 scanning electron microscope equipped with an electron backscatter diffraction (EBSD) camera were used in this investigation. A python-based routine was used to calculate the percentage of each phase based on at least three optical microscopy images on the microstructure images. From this routine, the average and associated standard deviations were determined. EBSD measurements were carried out using an acceleration voltage of 20 kV and a step size of 150 nm.

Hardness measurements were performed using a Mitutoyo HM-112 Hardness Testing Machine, under a load of 0.5 N for 10 s across the sample's total height, with a distance between indentations of 500 µm. Magnetic permeability measurements were performed using an absolute helicoidally shielded eddy current (EC) probe with a 3 mm diameter, operating in bridge mode [37]. The electrical impedance was calibrated with different magnetic permeability standards (ferrite samples), to distinguish between different materials with unknown magnetic permeabilities. The calibration was performed so that only the imaginary part of the electrical impedance of the probe conferred changes in the magnetic permeability of each sample. To measure the changes in electrical conductivity between samples, a four-point potential drop technique previously described in Sorger et al. [38] was used. Measurements were made across the full height, starting in the substrate. Because the selected heat treatments are expected to promote microstructure changes it is important to evaluate how other properties of interest evolve upon those heat treatment schedules. Both hardness and electrical conductivity measurements can provide an indirect sense of the microstructural changes across the heigh of the samples as a function of the selected heat treatment [17]. The probe has a needle spacing of 635 µm, and a current of 80 mA was imposed between the external needles.

Figure 3 details the position within a given WAAM wall where specimens were taken for microstructure and mechanical characterization.

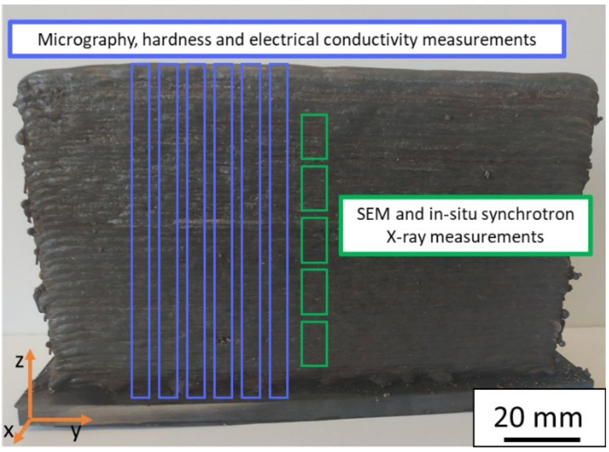

Figure 3 - Localization of the specimens taken from the Stainless steel 316 part, for microstructure and mechanical characterization.

3. Results and discussion

3.1 Macroscopic characterization

Figure 4 a) shows a micrograph of the as-built sample with primary dendrites composed of δ-ferrite aligned with the solidification direction (z-axis). Micrographs of the produced samples are depicted in Figure 4 b) to f). The as-built condition (Figure 4 b) is characterized by δ-ferrite dendrites oriented perpendicular to the deposition direction in an austenitic (γ) matrix. After the stress relief heat treatment, the microstructure maintained similar characteristics to that of the as-built condition (Figure 4 c). With the increase in the heat treatment temperature to 1050 °C, the columnar features became more unnoticeable, with the dissolution of dendrites arms (Figure 4 e). Finally, when the heat treatment was set to 1200 °C, almost no evidence of the original solidification microstructure of the as-built material exists. Only some tiny islands of residual ferrite dispersed in the matrix are depicted (refer to Figure 4 f).

Figure 4 a) depicts a variation in the morphology of ferrite as the number of layers increases. Typically, layers comprise skeletal-type ferrite in the non-remelted area and lathy-ferrite in the remelted area between layers [23,39], which is explained by the higher cooling rates in the remelted zone, since it is the first portion of volume to solidify [40].

Stainless steels solidify in one of four possible ways: mode A - single-phase austenite (Liquid → Liquid + γ → γ); mode AF - austenite with secondary ferrite (Liquid→ Liquid + γ → Liquid + γ + δ → γ + δ); mode FA - primary ferrite with secondary austenite (Liquid → Liquid + δ → Liquid + δ + γ → δ + γ); and mode F - single-phase Ferrite (Liquid → Liquid + δ → δ) [40]. The determination of the solidification mode can be based on the chromium to equivalent nickel ratio Cr_{eq}/Ni_{eq}. For the material used in this work, the Cr_{eq}/Ni_{eq} ratio is 1.69 and, considering Schaeffler's diagram, a ferritic-austenitic (FA) solidification mode is present. The solidification microstructure should be composed of austenite with a ferrite content ranging from 5 to 10 %. Under equilibrium solidification conditions, the austenitic stainless steel should present a ferritic-austenitic (FA) solidification mode, in which δ-ferrite is the leading phase, and austenite (γ) is the second phase that begins to form between the liquid and δ-ferrite dendrites in a peritectic reaction [41]. Austenite will continue to solidify from the rest of the melt afterward. The diffusion-controlled δ-ferrite to austenite transformation will continue during cooling and stop when the diffusion is no longer possible, resulting in a skeletal and lathy ferrite type [42].

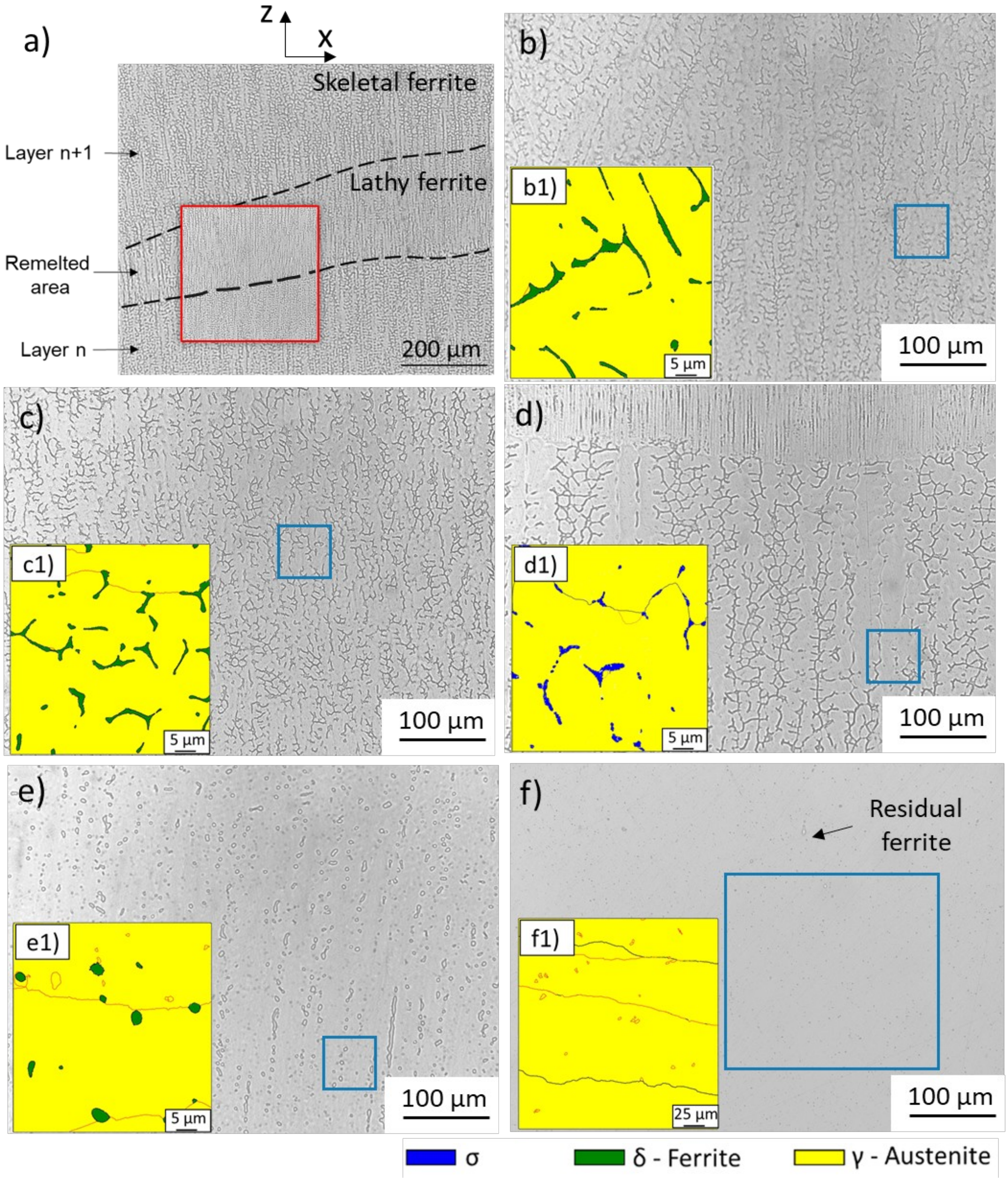

Figure 4 – a) and b) As-built, c) 400 °C 1h, d) 950 °C 2h, e) 1050 °C 2h f) 1200 °C 1h. Inserts b1, c1, d1, e1 and f1 correspond to the high magnification EBSD analysis.

3.2 Electron backscatter diffraction analysis

Figure 4 inserts depict the electron backscatter diffraction (EBSD) phase maps for each condition. As-built and stress relieved (400 °C / 1h) samples contain vermicular-type ferrite dispersed in the austenite matrix. The sample heat-treated at 950°C exhibits σ both in a vermicular-type structure and along the grain boundaries. The increase in the temperature to

1050 °C revealed a lower fraction and size of δ-ferrite, as only small islands are present. In the 1200 °C condition, δ completely disappeared from the WAAMed stainless steel part.

Sigma (σ) can take up to thousands of hours to precipitate directly from austenite [24]. Padilha et al. [44] found in a creep test performed at 600 °C, that σ precipitation in austenite only occurred after 5481 h. The following reasons explain the low kinetics of σ precipitation from austenite: i) low solubility of C and N within the σ, which causes carbides and nitrides to form instead of promoting the σ transformation; ii) very slow diffusion of substitutional elements in austenite; and iii) different crystal structures between σ and austenite, which hinders nucleation of the former. This lack of lattice coherence, as well as the high interfacial energy between both phases, is the reason that leads to increased interface cracking when σ is present in these materials [26]. Contrarily, the σ was found to precipitate very quickly from residual δ–ferrite [13]. It prefers high Cr-concentrated regions, present in higher quantities in δ–ferrite can diffuse easily in its BCC structure [45].

Perron et al. [19] proposed three mechanisms for the precipitation of σ: i) it involves nucleation at the γ/δ interface, which is a high interface energy site place beneficial for heterogeneous nucleation, and also a high Cr-region; ii) direct precipitation in the corners or triple points in the δ – ferrite, resulting from the Cr, Mo, and Ni concentration profiles; iii) eutectoid decomposition of δ-ferrite onto the σ and austenite (δ → σ + γ). Other nomenclatures exist; however, this partitioning is very similar to the one already described in the literature [26,46].

Due to the preservation of the ferrite vermicular-type showed in the micrographs and the EBSD maps (refer to Figure 4 d) it can be perceived that the appearance of σ results from direct precipitation on the δ-ferrite islands. By precipitating within the δ-ferrite, the σ consumes the Cr content and ultimately occupies the entire δ -ferrite islands.

The percentage of δ-ferrite and σ content was calculated from the optical microscope images previously depicted in Figure 4 with a Python routine, and the results are presented in Table 2. The percentage of δ–ferrite in the as-built sample, heat-treated at 400 °C, and heat-treated at 1050 °C sample, is respectively 16.9, 17, and 2.8 %. The percentage of σ in the sample heat-treated at 950 °C is around 16.8 %. Regarding the undissolved δ-ferrite in the sample heat-treated at 1200 °C, the δ–ferrite is below 0.5 %.

Table 2 – Phase percentage measurements made with a Python routine of each phase based on three different micrographs of each condition.

Condition	Austenite (γ)	δ-Ferrite	σ
As-built	83.1	16.9	-
400 °C 1h	83	17	-
950 °C 2h	83.2	-	16.8
1050 °C 2h	97.2	2.8	-
1200 °C 1h	99.5	0.5	-

3.3 Synchrotron X-ray diffraction analysis

3.3.1 Ex-situ microstructural characterization

Figure 5 depicts the diffraction patterns of the as-built sample and those after completion of the selected heat treatments. In the as-built sample, diffraction peaks corresponding to the austenite and ferrite phases are identified. Even though WAAM parts are kept at high temperatures for long periods during fabrication, no carbides or other undesirable phases than δ-ferrite were detected in the as-built sample.

Precipitation of σ was confirmed after two hours at 950 °C. Multiple diffraction peaks corresponding to σ are evidenced in the orange spectra of Figure 5. An apparent reduction in the intensity of the δ-ferrite peaks is observed after heat treatment at 1050 and 1200 °C. The insert in Figure 5 illustrates that δ-ferrite is still present after being heat-treated at 1050 °C.

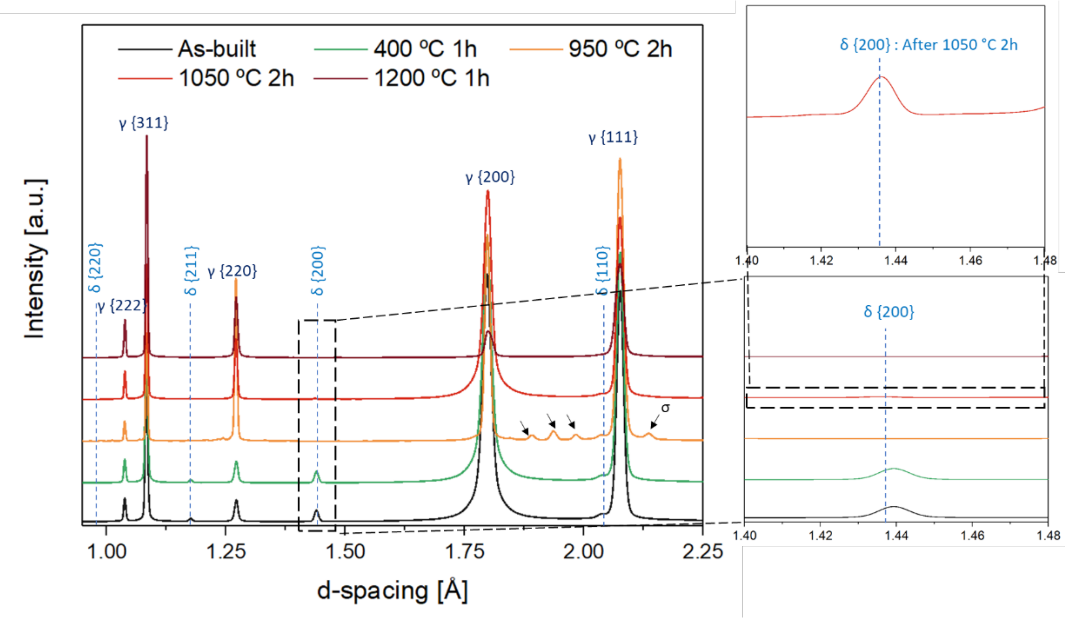

Figure 5 - Overview of the diffraction patterns of the as-built and heat-treated samples. Inserts illustrate the existence of δ-ferrite after being heat-treated for two hours at 1050 °C.

Table 3 shows the evolution of the d-spacing for several diffraction peaks of both austenite and ferrite phases after the stress-relief heat treatment. It is interesting to note the shift of both ferrite and austenite peaks to higher d-spacing values (or correspondingly to lower scattering angles), indicating a change in the microstrain state, as typically for post-processing heat treatments [47].

Table 3 - d-spacing values and lattice strain of the main austenite and δ-ferrite peaks before and after stress-relief heat treatment (400 °C for 1 h).

Peak	**d-spacing [Å]**	**d-spacing [Å]**	**Lattice strain**
	As-built	**Stress-relief**	
γ {311}	1.0835	1.0845	922
δ {211}	1.1742	1.1758	1362
γ {220}	1.2709	1.2714	393
δ {200}	1.4362	1.4397	2437
γ {200}	1.7967	1.7983	891
δ {110}	2.0413	2.0435	1078
γ {111}	2.0742	2.0810	3278

3.3.2 In-situ phase transformations

- Precipitation of σ from δ-ferrite at 950 °C

Figure 6 a) details the evolution of several diffracted σ planes ($\{202\}_{\sigma}$, $\{420\}_{\sigma}$, $\{411\}_{\sigma}$, and $\{311\}_{\sigma}$) during the first hour of isothermal holding at 950 °C. These results were retrieved after isolating portions of the spectra containing a large density of σ peaks. To obtain a kinetic observation of σ precipitation, intensity was normalized based on the last observed σ{411} peak intensity at the end of the isothermal stage. Notice that the intensity of σ peaks is too small to obtain reliable sequential fitting. Therefore, a semiquantitative approach to σ precipitation kinetics and dissolution of δ can be obtained by this method. In this experiment, it was observed that the σ started to precipitate during the first minute at isothermal holding. Qualitatively it was observed in Figure 6 a) that after 15 minutes of heat treatment at 950 °C, the $\{110\}_{\delta}$ peak disappeared and the $\{202\}_{\sigma}$ overlapped. However, due to the peak broadening of the σ reflection, which decreases over time, and due to the existence of $\{200\}_{\delta}$ peak after 60 minutes (refer to Figure 6 b), it is evidenced that the partial transformation of ferrite to σ was unfinished after 15 minutes.

The final amount of σ is highly dependent on the starting amount of δ-ferrite since σ preferentially forms in the δ-ferrite regions (Figure 4). These results highlight the importance of controlling the processing temperatures during WAAM to minimize the permanence times at high temperatures, hence preventing δ-ferrite amount and the precipitation of undesirable phases, such as σ, during subsequent heat treatments.

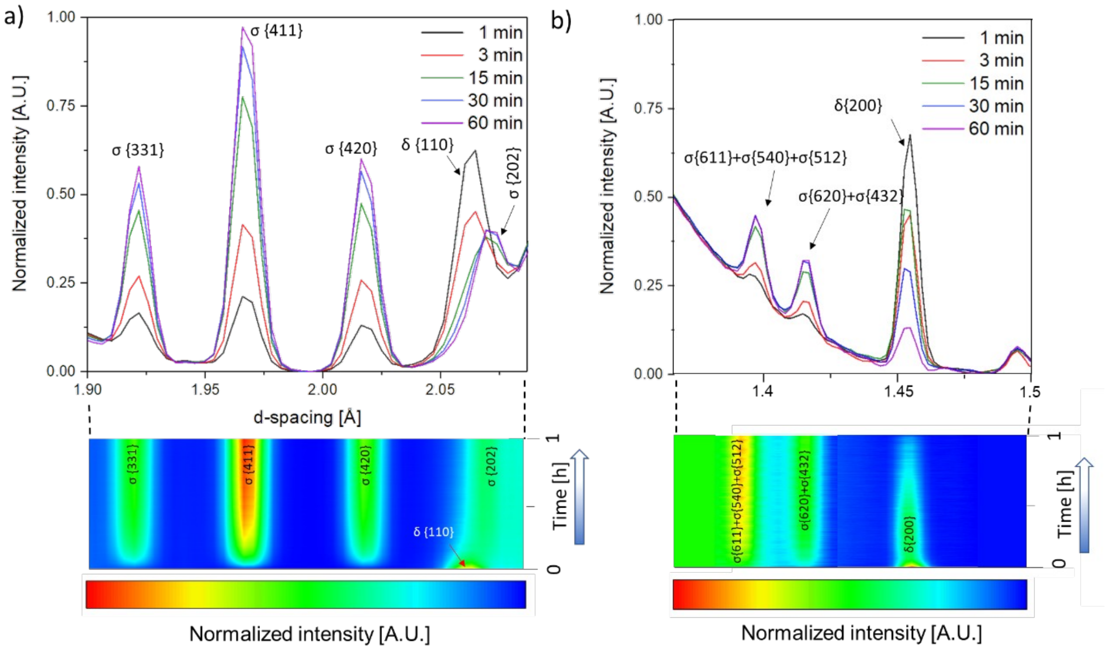

Figure 6 - a) and b)- Sigma (σ) growth and δ-ferrite dissolution in the isothermal stage at 950 °C after 1 min, 3 min, 15 min, 30 min, and 60 min. Peak intensity normalization of these two regions of the spectra (where a high density of σ peaks are observed) is conducted based on the maximum intensity of the $\{411\}_\sigma$ *peak. Therefore, green-to-red colors represent the relative kinetics of precipitation of σ, while blue denotes the constant normalized background counts.*

The dilatometry results of the first hour of the heat treatment performed at 950 °C are depicted in Figure 7. The peak intensity evolution is based on the normalized intensity plot shown in Figure 6 a). The observed behavior illustrates a slight contraction in the sample during the first hour of isothermal holding. Rivolta et al. [48] showed that σ precipitation from δ-ferrite leads to a slight contraction in the dilatometric curve. The increase in σ peak intensity and the continuous dissolution of δ ferrite indicate a constant transformation of δ to σ during the isothermal stage of the heat treatment at 950 °C. The fast kinetics of δ to σ transformation indicates that σ-growth is likely to be controlled by a small-scale atomic rearrangement of BCC into the tetragonal crystal structure, instead of long-range diffusion of substitutional alloying elements [49].

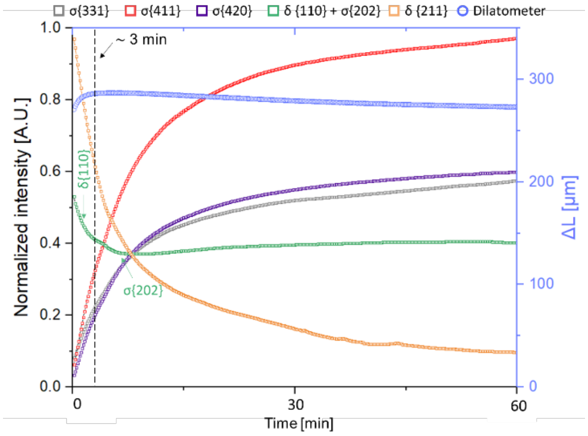

Figure 7 - Intensity evolution of the peaks $\{110\}_\delta$, $\{211\}_\delta$, $\{331\}_\sigma$, $\{411\}_\sigma$, $\{420\}_\sigma$ *and* $\{202\}_\sigma$ *during the first hour of the isothermal holding at 950 °C. The apparent stabilization of the* $\{110\}_\delta$ *peak after 3 minutes of isothermal dissolution is explained by the simultaneous precipitation of* $\{202\}_\sigma$ *This does not occur for* $\{110\}_\delta$ *The initial volumetric expansion is then associated with the dissolution of δ-ferrite. Precipitation of σ results in a modest volumetric contraction.*

After the two hours of heat treatment, no δ–ferrite peaks were found, as detailed in Figure 8 a). The large density of σ-phase precipitate peaks and the convolution of $\{110\}_\delta$ and $\{202\}_\sigma$ peaks are shown in a simulated XRD spectrum in Figure 8 b).

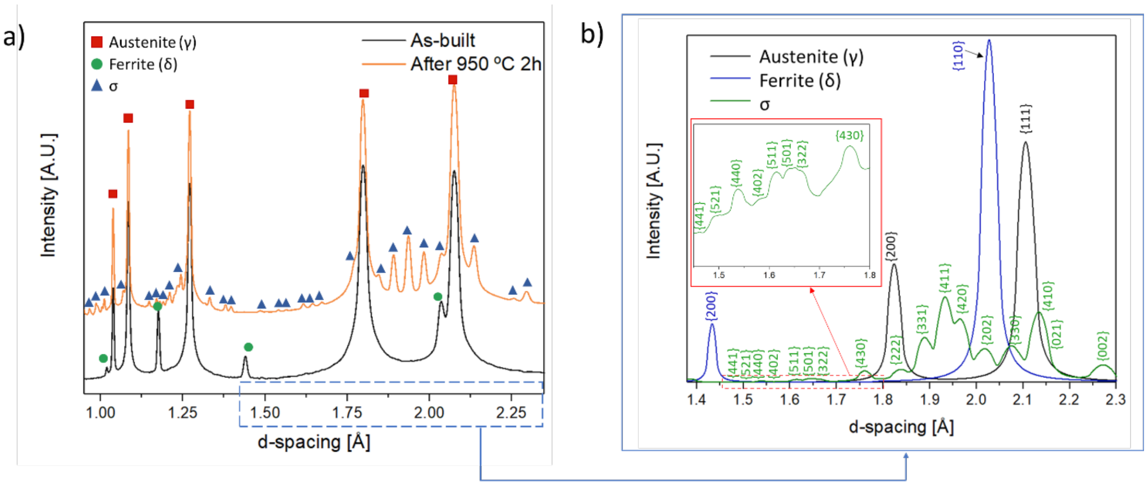

Figure 8 – a) Overall overview of the powder pattern before and after heat treatment for 2 hours at 950 °C.; b) Powder diffraction pattern of austenite, δ-ferrite, and σ.

- Dissolution of δ-ferrite at 1050 and 1200 °C

Figure 9 depicts the evolution of $\{111\}_{\gamma}$, $\{110\}_{\delta}$ and $\{200\}_{\delta}$ peaks during isothermal holding at 1050 °C for 120 minutes. The reduction in the scattered intensity of ferrite is accompanied by a decrease in the austenite reflection intensity. A texture change can explain this since no other compounds were formed during this heat treatment. Both solubilization heat treatments did not reveal any σ precipitation.

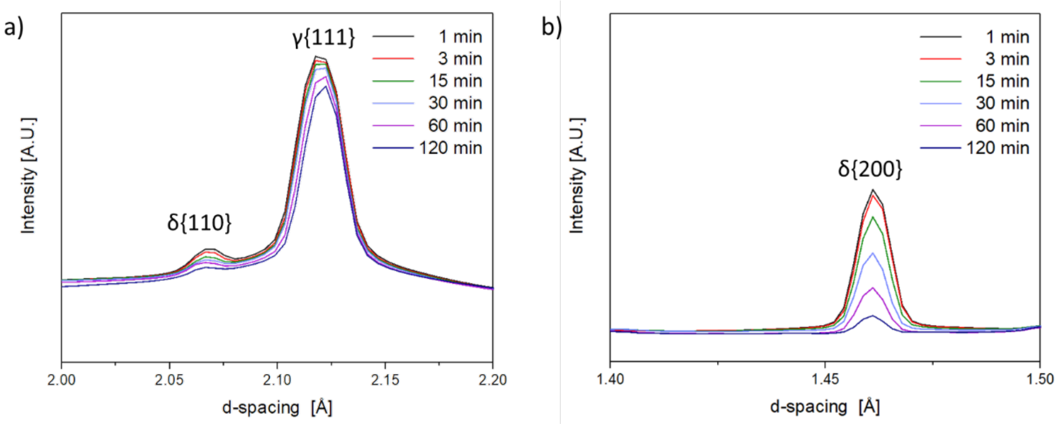

Figure 9 – δ-Ferrite dissolution after isothermal holding at 1050 °C for 1 min, 3 min, 15 min, 30 min, 60 min, and 120 min.

To monitor the dissolution of the ferrite during the post-WAAM heat treatments, the scattered intensity, full width at half maximum (FWHM), and area of the fitted peaks of the FCC reflections ($\{111\}_{\gamma}$, $\{200\}_{\gamma}$, $\{220\}_{\gamma}$, $\{311\}_{\gamma}$) and BCC reflections ($\{110\}_{\delta}$, $\{200\}_{\delta}$, $\{211\}_{\delta}$) were calculated to measure volume percent of austenite during heat treatment. It was determined that in the as-built condition, the amount of δ embed in the austenite matrix ranged between

84 and 89 % (refer to the starting point in Figure 10 a). These differences in the ferrite content can be explained by the recursive alternation between vermicular and lathy ferrite in the samples before heat treatment, which may vary the content of ferrite. So, if the beam is analyzing a slightly different region on the material, minor changes in the δ-ferrite amount can occur.

The volume percent of undissolved δ-ferrite was higher in the PWHT performed at 1050 °C than in the PWHT at 1200 °C (Figure 10 b). The undissolved amount of ferrite was approximately 6.5 % and 0.4 %, respectively. The continuous increase in the volume percent of austenite during isothermal holding at 1050 °C suggests that two hours were not enough to reach an equilibrium state, since thermodynamic equilibrium calculations (refer to Table 5) predict a complete dissolution of the ferrite phase at 1050 °C, and a residual amount of 2.6 % at 1200 °C. Two potential concurrent effects can explain this: i) the heat treatment time was not enough to reach an equilibrium condition; ii) the segregation of alloying elements during WAAM can locally change the material's chemistry, delaying the dissolution kinetics [50]. After solubilization at 1200 °C, only the stable $\{211\}_{\delta}$ peak is observed, indicating a texture modification.

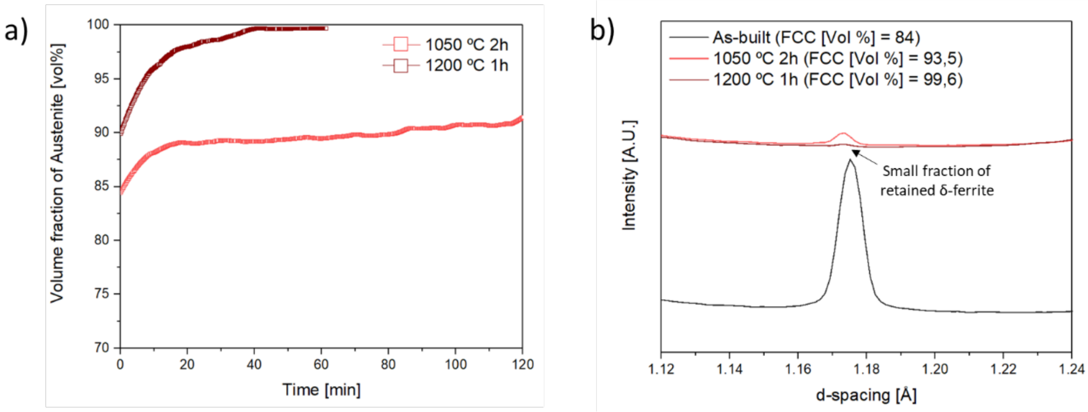

Figure 10 - a) Austenite volume percent during 1050 °C 2h and 1200 °C 1h; b) $\{200\}_{\delta}$ reflection before and after solubilization heat treatment.

The final fraction of δ-ferrite after the heat treatment decreases with an increase in the solubilization temperature. The complete dissolution of δ-ferrite in austenitic stainless steels can be hard to achieve since long heat treatment schedules are required [19,51].

Table 4 presents a comparison of the volume fraction measurements made using equations 1,2,3 vs the Rietveld refinement method. A maximum deviation of 0.62 % was measured, proving that the method used to measure the volume fraction when only two phases are presented is valid. Moreover with MAUD it was possible to calculate 15.7 % as the final volume fraction of σ in the sample heat-treated at 950 °C. The fact that the final volume fraction of σ (15.74 %) is practically the same as the initial δ-ferrite volume fraction measured for the as-built condition (15.75 %), allows us to conclude that δ-ferrite acted as a nucleation site for the precipitation of σ. The precipitation of σ was restricted to the δ-ferrite segregation zones, and no δ-ferrite dissolution to the austenite matrix occurred. These results are also in good agreement with the ones already presented in Table 2, which measured phase percentage based on the micrographs characteristics.

Table 4 – Comparison of the volume percent [%] of each phase after each heat treatment. Measurements were made via the single peak fitting method (equations:(1), (2) and (3)) vs Rietveld refinement method with MAUD.

Phase		Austenite		δ - Ferrite		σ	
Method		Single peak fitting	MAUD	Single peak fitting	MAUD	Single peak fitting	MAUD
Condition	As-built	83.75	84.25	16.25	15.75	n.a.	n.a.
	After 400 °C 1h	83.90	83.6	16.1	16.40	n.a.	n.a.
	After 950 °C 2h	Not measured	84.26	n.a.	n.a.	Not measured	15.74
	After 1050 °C 2h	93.5	94.12	6.5	5.88	n.a.	n.a.
	After 1200 °C 1h	99.7	99.54	0.3	0.46	n.a.	n.a.

The lattice parameters calculated from the lattice spacing (d-spacing) for different {hkl} planes are given for the higher intensity peaks of austenite in Figure 11. During isothermal holding at 1200 °C, the lattice parameter expands, which is attributed to the dissolution of ferrite that changes the austenite composition [52,53].

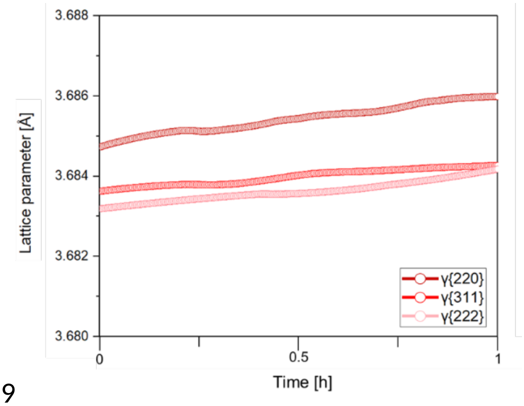

Figure 11 – Lattice parameter evolution of the most prominent FCC peaks during heat-treatment at 1200 °C.

Thermodynamic equilibrium calculations based on the TCFE11 database of Thermo-Calc (Table 5) were used to predict the equilibrium phases of the steel using the nominal composition in Table 1. Figure 12 depicts the equilibrium phase diagram with isopleths for each equilibrium phase as a function of temperature and the Cr mass percentage. Red crosses mark the ER 316LSi composition for each heat treatment temperature. It should be noticed that some discrepancies between the X-ray diffraction results and the equilibrium CalPhaD-based calculations exist. At 400 °C it is expected a 5% volume fraction of Laves, which was not found either by high-energy X-ray diffraction or microscopic analysis. Since the effect of each heat treatment largely depends on the initial microstructure, the thermodynamic calculations do not take into account the as-built microstructure of large δ-ferrite dendrites but rather the material's nominal composition, which at 400 °C hindered the formation of laves. Laves precipitation is very sluggish and may occur over extended heat treatment times at 400 °C. Padilha et al. [44] showed that Laves only precipitates at 550 °C after 10 000 hours. Additionally, σ is not expected to exist above 900 °C, thus the observed σ at 950 °C during and after the heat treatment is in a metastable equilibrium state. Since δ-ferrite is thermodynamically metastable at temperatures where the σ precipitates, σ will preferentially grow from within the δ-ferrite causing its decomposition [49]. When the temperature rises to 1050 and 1200 °C the system evolves into an equilibrium state by solubilizing the δ-ferrite. The experimentally observed residual δ-ferrite at 1050 and 1200 °C is not related to an equilibrium phase (formed above 1200 °C), but instead to insufficient decomposition. This can be explained since the selected heat treatment conditions are not equilibrium conditions: i. e. the chosen time for the post-WAAM heat treatment is not enough to reach an equilibrium condition.

Table 5 – Equilibrium calculations using TCFE11 database of Thermo-Calc for the volume percent [%] at the equilibrium temperatures of interest.

T [°C]	Austenite	δ - Ferrite	σ	Laves	$M_{23}C_6$
400 °C	72	23	-	5	-
950 °C	99.95	-	-	-	0.05
1050 °C	100	-	-	-	-
1200 °C	97.4	2.6	-	-	-

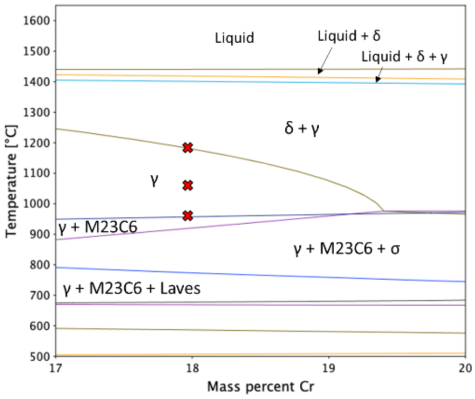

Figure 12 - Calculated isopleth for Cr mass percentage. The red crosses mark the composition of ER 316LSi at each heat treatment temperature. The thermodynamic information is taken from the commercial thermodynamic database TCFE11.

3.4 Hardness measurements

Vickers hardness plots as a function of distance from the substrate are presented in Figure 13. As it can be seen, the higher hardness corresponds to the as-built and stress relieved sample (400 °C 1h), ranging from 170 to 200 HV. Higher temperatures resulted in a more significant dissolution of δ-ferrite, and therefore in lower hardness values. A maximum of 174 HV is observed for the heat-treated sample at 1050 °C, while a maximum of 163 HV was found in samples heat-treated at 1200 °C. Even though there is none δ-ferrite on the sample heat-treated at 950 °C, the slight difference between the means of this sample with the as-built condition is explained by the similar hardness of the σ in comparison to that of δ-ferrite.

The stress-relieved sample had similar hardness values with the non-stress-relieved one and can be explained by the multiple thermal cycles developed during sample build-up. After one layer is built, it is subjected to considerable periods at temperatures between 300-500 °C, thus experiencing an in-situ (at least partial) stress-relieving mechanism during production. The more predominant variable to affect the hardness is, therefore, the amount of δ ferrite, as the hardness values obtained for the two different solubilization temperatures are lower than for the other heat treatment conditions

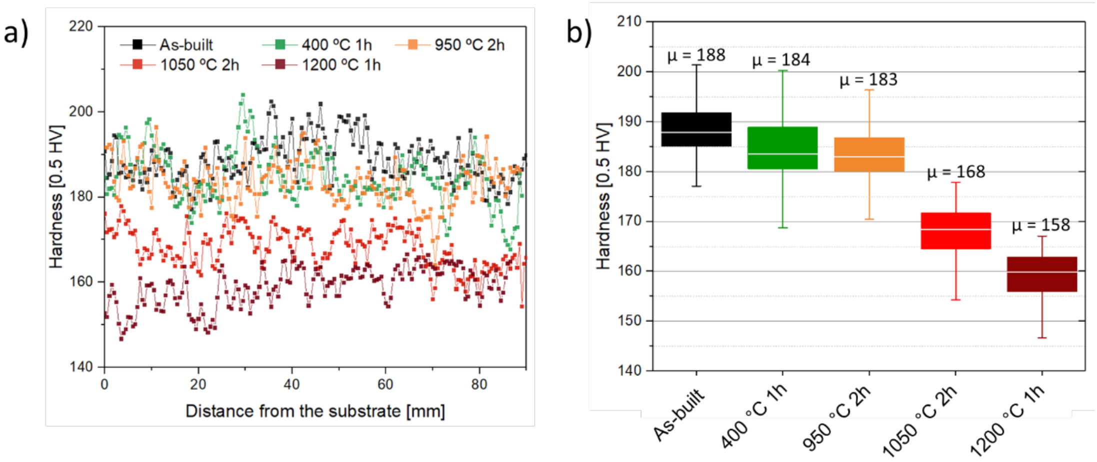

Figure 13 – a) Hardness measurements across sample's height, b) Boxplot of the hardness measurements displaying the minimum, maximum, median, and quartiles (Q1 and Q3) of each condition.

3.5 Electrical conductivity and magnetic permeability measurements

Eddy current testing (ECT) and four-point probe technique were used to evaluate magnetic permeability and electrical conductivity changes, respectively. Results are depicted in Figure 14. An inverse relation between the amount of δ-ferrite and the magnetic permeability was verified with ECT. With the gradual decrease of δ after PWHT at 1050 and 1200 °C, the signal output decreased. δ-ferrite is responsible to increase the magnetic permeability of the material, but sigma is not since it is not ferromagnetic. If there were not any X-ray diffraction measurements, δ-ferrite and σ could be qualitatively identified using ECT, as the microstructure images (Figure 4 b and d) do not allow to identify which constituents are present. The results show that the magnetic permeability of the samples containing δ (as-built and heat-treated at 400 °C for 1h) is three times higher than the sample that includes the σ (heat-treated at 950 °C 2h). The technique is very sensitive to variations of magnetic pearmeability, thus, variations in the δ-ferrite amount, however, very small variations of the electrical impedance were measured, as shown in Figure 14 b).

The average measurements of the electrical conductivity of these samples are between 2.169 and 2.209 %IACS. The high standard deviation does not allow to establish any relationship between the amount of ferrite in a sample and the phases in it or with the grain size.

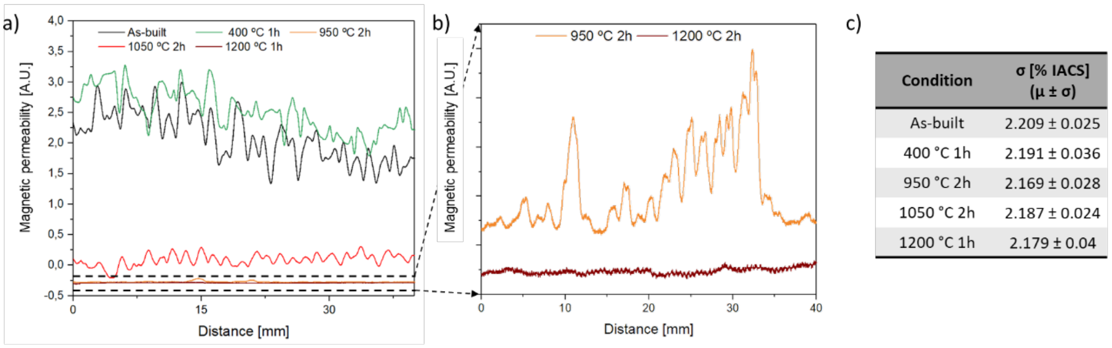

Condition	σ [% IACS] (μ ± σ)
As-built	2.209 ± 0.025
400 °C 1h	2.191 ± 0.036
950 °C 2h	2.169 ± 0.028
1050 °C 2h	2.187 ± 0.024
1200 °C 1h	2.179 ± 0.04

Figure 14 - a) Output signal of Eddy Current Testing (ECT) probe at 1.1 MHz, b) Detailed view of the signal output of ECT delineated with dashed lines, c) Average electrical conductivity measurements with a four-point probe for each condition.

Conclusions

A comprehensive study on the effect of post-WAAM heat treatments applied on 316L stainless steel was performed. By combining advanced microstructure characterization and in-situ measurements the following are the major findings of this work:

- The as-built WAAM samples presented an austenitic matrix with skeletal-type δ-ferrite and lathy-ferrite aligned with the solidification direction (z-axis). No other secondary phases were discernible.
- After the stress relief at 400°C, the microstructure retained similar characteristics to that of the as-built condition. Synchrotron X-ray diffraction showed that both the δ-ferrite and austenite peaks shifted to lower scattering angles, evidencing a change in microstrain. This heat treatment decreased the sample hardness by an average of 4 HV.
- There is no clear morphological difference between the as-built sample and sample heat-treated at 950 °C for two hours. However, by electron backscatter diffraction, it was confirmed that δ-ferrite acted as a nucleation site for the precipitation of undesirable σ-phase. The precipitation of the σ-phase was geometrically restricted to the δ-ferrite segregation zones.
- In-situ observations showed that σ precipitation started within the first minutes of isothermal holding at 950 °C, and two hours was enough to fully transform δ → σ. A hardness decreased of 5 HV relative to the as-built sample was achieved.

- Thermodynamic calculations do not predict the existence of σ in the sample heat-treated at 950 °C. Insufficient kinetics for δ-ferrite dissolution led to a metastable equilibrium condition, where σ replaced the former vermicular δ-ferrite structures
- A temperature of 1050 °C showed to be enough to promote ferrite dissolution and compositional redistribution into the austenitic matrix, avoiding the precipitation of metastable σ. Efficient dissolution of δ-ferrite dendrites can be achieved with higher solubilization temperature, as heat treatments performed at 1050 and 1200 °C resulted in approximately 6.5 % and 0.4 % of δ-ferrite, respectively.
- Eddy's current testing was shown to be able to distinguish σ from δ-ferrite in the stainless steel WAAM parts. These results are promising for in-situ inspections of large as-built components that cannot be easily segmented or transported.

Acknowledgments

TAR acknowledges FCT - MCTES for funding the Ph.D. grant SFRH/BD/144202/2019. VD acknowledges FCT - MCTES for funding the Ph.D. grant SFRH/BD/139454/2018. TAR, JS, VD, TGS, and JPO acknowledge Fundação para a Ciência e a Tecnologia (FCT - MCTES) for its financial support via the project UID/00667/2020 (UNIDEMI). The São Paulo Research Foundation partially financed this study (FAPESP), grant No. 2019/00691-0. The authors acknowledge DESY (Hamburg, Germany), a member of the Helmholtz Association HGF, for the provision of experimental facilities. Beamtime was allocated for proposals I-20181084 EC and I-20191506. The research leading to this result has been supported by the project CALIPSOplus under the Grant Agreement 730872 from the EU Framework Programme for Research and Innovation HORIZON 2020.

References

[1] S.J. Zinkle, G.S. Was, Materials challenges in nuclear energy, Acta Mater. 61 (2013) 735–758. https://doi.org/https://doi.org/10.1016/j.actamat.2012.11.004.

[2] S.K. Lee, S.H. Yun, H.G. Joo, S.J. Noh, Deuterium transport and isotope effects in type 316L stainless steel at high temperatures for nuclear fusion and nuclear hydrogen technology applications, Curr. Appl. Phys. 14 (2014) 1385–1388. https://doi.org/10.1016/j.cap.2014.08.006.

[3] M. Ziętala, T. Durejko, M. Polański, I. Kunce, T. Płociński, W. Zieliński, M. Łazińska, W. Stępniowski, T. Czujko, K.J. Kurzydłowski, Z. Bojar, The microstructure, mechanical properties and corrosion resistance of 316 L stainless steel fabricated using laser engineered net shaping, Mater. Sci. Eng. A. 677 (2016) 1–10. https://doi.org/10.1016/j.msea.2016.09.028.

[4] Y. Dai, X. Zheng, P. Ding, Review on sodium corrosion evolution of nuclear-grade 316 stainless steel for sodium-cooled fast reactor applications, Nucl. Eng. Technol. 53 (2021) 3474–3490. https://doi.org/10.1016/j.net.2021.05.021.

[5] Q. He, F. Pan, D. Wang, H. Liu, F. Guo, Z. Wang, Y. Ma, Microstructure and properties of 316L stainless steel foils for pressure sensor of pressurized water reactor, Nucl. Eng. Technol. 53 (2021) 172–177. https://doi.org/10.1016/j.net.2020.06.006.

[6] R.K. Desu, H. Nitin Krishnamurthy, A. Balu, A.K. Gupta, S.K. Singh, Mechanical properties of Austenitic Stainless Steel 304L and 316L at elevated temperatures, J. Mater. Res. Technol. 5 (2016) 13–20. https://doi.org/https://doi.org/10.1016/j.jmrt.2015.04.001.

[7] H.P. Seifert, S. Ritter, H.J. Leber, Corrosion fatigue crack growth behaviour of austenitic stainless steels under light water reactor conditions, Corros. Sci. 55 (2012) 61–75. https://doi.org/10.1016/j.corsci.2011.10.005.

[8] F.L. Xu, J.Z. Duan, C.G. Lin, B.R. Hou, Influence of Marine Aerobic Biofilms on Corrosion of 316L Stainless Steel, J. Iron Steel Res. Int. 22 (2015) 715–720. https://doi.org/10.1016/S1006-706X(15)30062-5.

[9] M.M. DEWIDAR, K.A. KHALIL, J.K. LIM, Processing and mechanical properties of porous 316L stainless steel for biomedical applications, Trans. Nonferrous Met. Soc. China (English Ed. 17 (2007) 468–473. https://doi.org/10.1016/S1003-6326(07)60117-4.

[10] X. Lou, M.A. Othon, R.B. Rebak, Corrosion fatigue crack growth of laser additively-manufactured 316L stainless steel in high temperature water, Corros. Sci. 127 (2017) 120–130. https://doi.org/10.1016/j.corsci.2017.08.023.

[11] J.P. Oliveira, T.G. Santos, R.M. Miranda, Revisiting fundamental welding concepts to improve additive manufacturing: From theory to practice, Prog. Mater. Sci. 107 (2020) 100590. https://doi.org/10.1016/j.pmatsci.2019.100590.

[12] V.R. Duarte, T.A. Rodrigues, N. Schell, R.M. Miranda, J.P. Oliveira, T.G. Santos, Hot Forging Wire and Arc Additive Manufacturing (HF-WAAM), Addit. Manuf. (2020) 101193. https://doi.org/10.1016/j.addma.2020.101193.

[13] J.A. Brooks, F.J. Lambert, Effects of Phosphorus, Sulfur and Ferrite Content on Weld Cracking of Type 309 Stainless Steel., Weld. J. (Miami, Fla). 57 (1978).

[14] A. Ben Rhouma, T. Amadou, H. Sidhom, C. Braham, Correlation between microstructure and intergranular corrosion behavior of low delta-ferrite content AISI 316L aged in the range 550–700 °C, J. Alloys Compd. 708 (2017) 871–886. https://doi.org/10.1016/j.jallcom.2017.02.273.

[15] J.C. Lippold, W.F. Savage, Solidification of Austenitic Stainless Steel Weldments - 3. the Effect of Solidification Behavior on Hot Cracking Susceptibility., Weld. J. (Miami, Fla). 61 (1982) 388–396.

[16] P.D. Jablonski, J.A. Hawk, Homogenizing Advanced Alloys: Thermodynamic and Kinetic Simulations Followed by Experimental Results, J. Mater. Eng. Perform. 26 (2017) 4–13. https://doi.org/10.1007/s11665-016-2451-3.

[17] T.A. Rodrigues, V. Duarte, J.A. Avila, T.G. Santos, R.M. Miranda, J.P. Oliveira, Wire and arc additive manufacturing of HSLA steel: Effect of thermal cycles on microstructure and mechanical properties, Addit. Manuf. 27 (2019). https://doi.org/10.1016/j.addma.2019.03.029.

[18] T.F. de Andrade, A.M. Kliauga, R.L. Plaut, A.F. Padilha, Precipitation of Laves phase in a 28%Cr-4%Ni-2%Mo-Nb superferritic stainless steel, Mater. Charact. 59 (2008) 503–507. https://doi.org/10.1016/j.matchar.2007.03.006.

[19] A. Perron, C. Toffolon-Masclet, X. Ledoux, F. Buy, T. Guilbert, S. Urvoy, S. Bosonnet, B. Marini, F. Cortial, G. Texier, C. Harder, V. Vignal, P. Petit, J. Farré, E. Suzon, Understanding sigma-phase precipitation in a stabilized austenitic stainless steel (316Nb) through complementary CALPHAD-based and experimental investigations, Acta Mater. 79 (2014) 16–29. https://doi.org/10.1016/j.actamat.2014.06.066.

[20] M.J. Cieslak, A.M. Ritter, W.F. Savage, Chi-Phase Formation During Soldification and Cooling of Cf-8M Weld Metal., Weld. J. (Miami, Fla). 63 (1984).

[21] A.D. Warren, I.J. Griffiths, P.E.J. Flewitt, Precipitation within localised chromium-enriched regions in a Type 316H austenitic stainless steel, J. Mater. Sci. 53 (2018) 6183–6197. https://doi.org/10.1007/s10853-017-1748-4.

[22] D.M. Escriba, E. Materna-Morris, R.L. Plaut, A.F. Padilha, Chi-phase precipitation in a duplex stainless steel, Mater. Charact. 60 (2009) 1214–1219. https://doi.org/10.1016/j.matchar.2009.04.013.

[23] X. Chen, J. Li, X. Cheng, B. He, H. Wang, Z. Huang, Microstructure and mechanical properties of the austenitic stainless steel 316L fabricated by gas metal arc additive manufacturing, Mater. Sci. Eng. A. 703 (2017) 567–577. https://doi.org/10.1016/j.msea.2017.05.024.

[24] P. Long, D. Wen, J. Min, Z. Zheng, J. Li, Y. Liu, Microstructure evolution and mechanical properties of a wire-arc additive manufactured austenitic stainless steel: Effect of processing parameter, Materials (Basel). 14 (2021). https://doi.org/10.3390/ma14071681.

[25] D.M.E. Villanueva, F.C.P. Junior, R.L. Plaut, A.F. Padilha, Comparative study on sigma phase precipitation of three types of stainless steels: Austenitic, superferritic and duplex, Mater. Sci. Technol. 22 (2006) 1098–1104. https://doi.org/10.1179/174328406X109230.

[26] C.-C. Hsieh, W. Wu, Overview of Intermetallic Sigma () Phase Precipitation in Stainless Steels, ISRN Metall. 2012 (2012) 1–16. https://doi.org/10.5402/2012/732471.

[27] K.W. Chan, S.C. Tjong, Effect of secondary phase precipitation on the corrosion behavior of duplex stainless steels, Materials (Basel). 7 (2014) 5268–5304. https://doi.org/10.3390/ma7075268.

[28] V.S. Raghunathan, V. Seetharaman, S. Venkadesan, P. Rodriguez, The influence of post weld heat treatments on the structure, composition and the amount of ferrite in type 316 stainless steel welds, Metall. Trans. A. 10 (1979) 1683–1689. https://doi.org/10.1007/BF02811701.

[29] C. Arganis, N.F. Garza-montes-de-oca, Original article Sensitization of an austenitic stainless steel due to the occurrence of δ -ferrite, (2018). https://doi.org/10.1515/corrrev-2018-0036.

[30] Q. Chao, S. Thomas, N. Birbilis, P. Cizek, P.D. Hodgson, D. Fabijanic, The effect of post-processing heat treatment on the microstructure, residual stress and mechanical properties of selective laser melted 316L stainless steel, Mater. Sci. Eng. A. 821 (2021) 141611. https://doi.org/10.1016/j.msea.2021.141611.

[31] N. Chen, G. Ma, W. Zhu, A. Godfrey, Z. Shen, G. Wu, X. Huang, Enhancement of an additive-manufactured austenitic stainless steel by post-manufacture heat-treatment, Mater. Sci. Eng. A. 759 (2019) 65–69. https://doi.org/10.1016/j.msea.2019.04.111.

[32] D. Kong, C. Dong, X. Ni, L. Zhang, J. Yao, C. Man, X. Cheng, K. Xiao, X. Li, Mechanical properties and corrosion behavior of selective laser melted 316L stainless steel after different heat treatment processes, J. Mater. Sci. Technol. 35 (2019) 1499–1507. https://doi.org/10.1016/j.jmst.2019.03.003.

[33] A.N.F.& D.H. A. P. Hammersley, S. O. Svensson, M. Hanfland, Two-dimensional detector software: From real detector to idealised image or two-theta scan, High Press. Res. 14:4–6 (1996) 235–248. https://doi.org/10.1080/08957959608201408.

[34] P. Crowther, C. Daniel, xrdfit: A Python package for fitting synchrotron X-ray diffraction spectra, J. Open Source Softw. 5 (2020) 2381. https://doi.org/10.21105/joss.02381.

[35] J.D. Escobar, G.A. Faria, L. Wu, J.P. Oliveira, P.R. Mei, A.J. Ramirez, Austenite reversion kinetics and stability during tempering of a Ti-stabilized supermartensitic stainless steel: Correlative in situ synchrotron x-ray diffraction and dilatometry, Acta Mater. 138 (2017) 92–99. https://doi.org/10.1016/j.actamat.2017.07.036.

[36] L. Lutterotti, R. Vasin, H.R. Wenk, Rietveld texture analysis from synchrotron diffraction images. I. Calibration and basic analysis, Powder Diffr. 29 (2014) 76–84. https://doi.org/10.1017/S0885715613001346.

[37] T.G. Santos, R.M. Miranda, P. Vilaça, J.P. Teixeira, J. dos Santos, Microstructural mapping of friction stir welded AA 7075-T6 and AlMgSc alloys using electrical conductivity, Sci. Technol. Weld. Join. 16 (2011) 630–635. https://doi.org/10.1179/1362171811Y.0000000052.

[38] G.L. Sorger, J.P. Oliveira, P.L. Inácio, N. Enzinger, P. Vilaça, R.M. Miranda, T.G. Santos, Non-destructive microstructural analysis by electrical conductivity: Comparison with hardness measurements in different materials, J. Mater. Sci. Technol. 35 (2019) 360–

368. https://doi.org/10.1016/j.jmst.2018.09.047.

[39] E.G. Astafurova, M.Y. Panchenko, V.A. Moskvina, G.G. Maier, S. V. Astafurov, E. V. Melnikov, A.S. Fortuna, K.A. Reunova, V.E. Rubtsov, E.A. Kolubaev, Microstructure and grain growth inhomogeneity in austenitic steel produced by wire-feed electron beam melting: the effect of post-building solid-solution treatment, J. Mater. Sci. 55 (2020) 9211–9224. https://doi.org/10.1007/s10853-020-04424-w.

[40] J.W. Elmer, S.M. Allen, T.W. Eagar, Microstructural development during solidification of stainless steel alloys, Metall. Trans. A. 20 (1989) 2117–2131. https://doi.org/10.1007/BF02650298.

[41] N. Suutala, T. Takalo, Austenitic Stainless Steel Welds, Metall. Trans. A. l (1980) 717–725.

[42] J.W. Fu, Y.S. Yang, J.J. Guo, Formation of a blocky ferrite in Fe-Cr-Ni alloy during directional solidification, J. Cryst. Growth. 311 (2009) 3661–3666. https://doi.org/10.1016/j.jcrysgro.2009.05.007.

[43] A. F. PADILHA, P. R. RIOS, Decomposition of Austenite in Austenitic Stainless Steels, ISIJ Int. 42 (2002) 325–337.

[44] A.F. Padilha, D.M. Escriba, E. Materna-Morris, M. Rieth, M. Klimenkov, Precipitation in AISI 316L(N) during creep tests at 550 and 600 °C up to 10 years, J. Nucl. Mater. 362 (2007) 132–138. https://doi.org/10.1016/j.jnucmat.2006.12.027.

[45] J.R.Y. T.H. Chen, Effects of solution treatment and continuous cooling on |-phase precipitation in a 2205 duplex stainless steel, 311 (2006) 220.

[46] J.W. Elmer, T.A. Palmer, E.D. Specht, Direct observations of sigma phase formation in duplex stainless steels using In-situ synchrotron X-ray diffraction, Metall. Mater. Trans. A Phys. Metall. Mater. Sci. 38 (2007) 464–475. https://doi.org/10.1007/s11661-006-9076-3.

[47] J.P. Oliveira, F.M.B. Fernandes, R.M. Miranda, N. Schell, J.L. Ocaña, Residual stress analysis in laser welded NiTi sheets using synchrotron X-ray diffraction, Mater. Des. 100 (2016) 180–187. https://doi.org/10.1016/j.matdes.2016.03.137.

[48] B. Rivolta, R. Gerosa, F. Tavasci, The dilatometric technique for studying sigma phase precipitation kinetics in F55 steel grade, J. Therm. Anal. Calorim. 132 (2018) 869–877.

https://doi.org/10.1007/s10973-017-6940-x.

[49] S. Atamert, J.E. King, Sigma-phase formation and its prevention in duplex stainless steels, J. Mater. Sci. Lett. 12 (1993) 1144–1147. https://doi.org/10.1007/BF00420548.

[50] A. Caballero, J. Ding, S. Ganguly, S. Williams, Wire + Arc Additive Manufacture of 17-4 PH stainless steel: Effect of different processing conditions on microstructure, hardness, and tensile strength, J. Mater. Process. Technol. 268 (2019) 54–62. https://doi.org/10.1016/j.jmatprotec.2019.01.007.

[51] T.P.S. Gill, M. Vijayalakshmi, J.B. Gnanamoorthy, K.A. Padmanabhan, Transformation of Delta-Ferrite During the Postweld Heat Treatment of Type 316L Stainless Steel Weld Metal., Weld. J. (Miami, Fla). 65 (1986) 122–128.

[52] A. Bénéteau, P. Weisbecker, G. Geandier, E. Aeby-Gautier, B. Appolaire, Austenitization and precipitate dissolution in high nitrogen steels: An in situ high temperature X-ray synchrotron diffraction analysis using the Rietveld method, Mater. Sci. Eng. A. 393 (2005) 63–70. https://doi.org/10.1016/j.msea.2004.09.054.

[53] D. Manova, S. Mändl, H. Neumann, B. Rauschenbach, Analysis of in situ XRD measurements for low energy ion beam nitriding of austenitic stainless steel, Surf. Coatings Technol. 256 (2014) 64–72. https://doi.org/10.1016/j.surfcoat.2014.03.047.